International Journal of Pharmaceutics 426 (2012) 108–115

Contents lists available at SciVerse ScienceDirect

International Journal of Pharmaceutics

journal homepage: www.elsevier.com/locate/ijpharm

Distribution of aerosols in mouse lobes by fluorescent imaging

Dandan Yi[a,1], Amir Naqwi[b,2], Angela Panoskaltsis-Mortari[c], Timothy Scott Wiedmann[a,*]

[a] Department of Pharmaceutics, University of Minnesota, Minneapolis, MN 55455, United States
[b] Powerscope Incorporated, 1313 Fifth Street SE, Minneapolis, MN 55414, United States
[c] Pediatric BMT and Pulmonary Medicine, University of Minnesota, Minneapolis, MN 55455, United States

ARTICLE INFO

Article history:
Received 25 October 2011
Received in revised form 13 January 2012
Accepted 15 January 2012
Available online 25 January 2012

Keywords:
Fluorescent imaging
Lungs
Aerosol
Aluminum phthalocyanine tetrasulfonic acid
Aerosol distribution

ABSTRACT

Better methods are needed to quantify the distribution of drug among the airways of the lungs of small animals to facilitate the development of agents that can target specific airways. Mice were exposed to aerosols of aluminum phthalocyanine tetrasulfonic acid (AlPCS) that ranged in concentration and size (0.2–2.8 μm). The trachea and lobes were removed and placed between glass slides, and fluorescent images were obtained at two different compression thicknesses. The intensity, normalized by the area, exposure time, and thickness, was then plotted as a function of compression thickness, from which the concentration and attenuation coefficient were estimated for each lobe and then for each pixel of the image. The latter was then used to generate an image reflective of the concentration. The lobe volume, concentration, and tissue attenuation of AlPCS was consistent among the lobes. The deposition fraction increased with decreasing particle size. The network of lines in the concentration image indicated that connective tissue has a lower concentration. The central airways were clearly evident in the images of mice exposed to the very small and large aerosols. This approach provides a rapid, economical means to obtain high resolution images of mouse lungs from which detailed analysis of the distribution of deposited aerosol particles can be obtained.

1. Introduction

Respiratory delivery is an effective means to achieve a high localized concentration of drug in the lungs. This principle has been exploited to improve patient care in a number of disease states with asthma perhaps being the most well known. However, as the understanding of disease processes grows, there is a desire to further direct the drug to specific areas in the lower respiratory tract (Eberl et al., 2006; Martin et al., 2008; Dolovich, 2009; Weers et al., 2009; Rostami, 2009; Jaafar-Maalej et al., 2009). For example in lung cancer, adenocarcinoma largely occurs in the lung periphery, whereas squamous cell carcinoma is often limited to the larger conducting airways (Adams et al., 2007). Preferential drug deposition in the respective areas for these diseases would improve efficacy and reduce toxicity. Asthma, chronic obstructive pulmonary disease, pulmonary hypertension, and bronchiolitis obliterans syndrome are also lung diseases that may benefit from a more localized delivery of drug (Xie et al., 2008). Thus, the current efforts to develop efficacious agents now also coincide with an interest to target the airways that would maximize drug delivery to the affected tissues (Yi et al., 2010). For this purpose, methods are needed to quantify the distribution of drug among the airways in small animals.

Assessing the distribution of particles within the lung in a quantitative manner is a challenging problem (Martin et al., 2008; Weers et al., 2009; Jaafar-Maalej et al., 2009). In essence, two measurements are required. One is the spatial distribution of the deposited particles, and another is a characterization of the spatial distribution of the lung airways. These measured distributions must be linked, so that the deposited drug can be assigned to the type of airway or generation where it resides (Rostami, 2009). Previously, we used fluorescent imaging to assess the distribution of particles among the lobes of the mouse lung (Yi et al., 2010). The technique was chosen in preference to more sophisticated approaches, such as PET (Dolovich, 2009), SPECT (Rostami, 2009), or MRI (Martin et al., 2008), due to its widespread availability, low cost, and ready application to smaller animal models. Fluorescent imaging was used as a means to determine the fluorophore concentration in each mouse lung lobe (Yi et al., 2010). The use of the probe, AlPCS, permitted measurements of the excitation and emission wavelengths in the near-infrared region where biological tissue auto-fluorescence is negligible and tissue attenuation is minimal (Chen et al., 2006;

* Corresponding author at: Department of Pharmaceutics, University of Minnesota, 308 Harvard Street SE, Minneapolis, MN 55455, United States.
Tel.: +1 612 624 5457; fax: +1 612 626 2125.
E-mail addresses: yixxx106@umn.edu (D. Yi), anaqwi@powerscopetech.com (A. Naqwi), wiedm001@umn.edu (T.S. Wiedmann).
[1] Tel.: +1 612 624 7968; fax: +1 612 626 2125.
[2] Tel.: +1 612 331 4247; fax: +1 612 623 3928.

0378-5173/$ – see front matter © 2012 Elsevier B.V. All rights reserved.
doi:10.1016/j.ijpharm.2012.01.037

Ntziachristos et al., 2008; Comsa et al., 2008; Mohajerani et al., 2009). In addition, the relationship between the intensity within a pixel and the number of fluorescent molecules within the rectangular prism was established by empirically accounting for absorption of light by tissue. While the deposition of AlPCS in each lobe was quantitatively determined, this did not significantly advance the goal of determining the distribution of drugs within the air ways of varying dimensions in a given lobe.

In this work, the distribution of the fluorescent probe among mouse lobes was examined following exposure of mice to aerosols with different particle size distributions. Using the above approach, the concentration of the fluorophore in each lobe was quantified. While the deposition fraction varied with particle size, there was no significant effect on the concentration of drug in the different lobes. Extending the previous approach for measuring the deposition in each lobe, the concentration within each pixel was estimated. By comparing images of intensity with those generated based on the concentration, the latter appeared more uniform reflecting the correction for tissue attenuation. In comparing the aerosols with different particle size distributions, the intermediate particle size aerosols appeared to provide the most uniform distribution of fluorescent probe.

2. Materials and methods

Aluminum (III) phthalocyanine chloride tetrasulfonic acid (AlPCS) was purchased from Frontier Scientific, Inc., Woburn, MA, USA. Water used in these experiments was deionized, distilled and deoxygenated. Gas cylinders of air were obtained from Minneapolis Oxygen Company (Minneapolis, MN, USA).

To examine the effect of particle size on the deposition pattern, data from the previous work in which exposures were carried out with a modified Medi-Nuclear (M-N) jet nebulizer (Powerscope Inc., Minneapolis, MN, USA) was analyzed. The M-N jet nebulizer was operated at 30 psi with a compressor and contained either a 10 mg/ml solution AlPCS alone or a combined solution of 10 mg/ml AlPCS and 100 mg/ml CsCl. As reported earlier, the particle size distribution was measured with a scanning mobility particle sizer (SMPS) (TSI, Minneapolis, MN, USA). The observed number distribution was converted to a mass distribution by assuming a density of 1 g/ml for the pure dye aerosol and 4 g/ml of the dye/CsCl aerosol. In addition, the output rate was determined by the filter capture method, extracting the filters and then imaging the extract solutions. The concentration was interpolated from a standard curve based on the results of imaging the extraction solution of spiked filters with a known mass of AlPCS. From the latter measurement, the mass output rate (mass/time) was converted to an aerosol concentration (mass/volume of air) by dividing by the air flow rate, 2 LPM. This data is summarized in Table 1.

Three additional exposures were conducted with an aerosol generated by an ultrasonic atomizer operating at a nominal frequency of 1.9 MHz with and without a drying column. For these, an ultrasonic (US) atomizer was used that operated with an air flow rate of 0.5 LPM, and in each case the baffle contained an AlPCS solution of 2 mg/ml. A schematic of the system has been published previously (Xie et al., 2010). One aerosol consisted of the unmodified droplets, a second aerosol consisted of dry particles that were obtained by passing the droplets through a drying column. The third aerosol was produced by adding 18 mg/ml CsCl to the dye solution and passing the droplets through the same drying column. The concentration of AlPCS was thus adjusted among the different nebulizers to allow the capture of images of comparable fluorescent intensity, despite the variation in the output of the different nebulizers and lung deposition. For these particles, the size distribution was determined with an Intox low flow rate cascade impactor operating at 0.5 LPM. The relative mass AlPCS collected on each stage was determined by imaging the solutions obtained from extracting the impactor plates with water. The output rate was determined by the filter capture method as described above.

Deposition experiments were carried out with five different aerosols as noted above. Female C57BL/6N inbred mice (6–7 weeks, 19–21 g) were purchased from Harlan Sprague Dawley, Inc. (Indianapolis, IN, USA) and handled in accordance to an approved protocol, University of Minnesota. The mice were allowed food and water prior to aerosol exposure. For exposures, conscious mice were restrained by hand during the nose-only exposure of 1 min. The mice were then sacrificed by cervical dislocation immediately after aerosol exposure. The lung was severed at the carina, and the trachea and lung were removed and then the lung divided into lobes. The lobes were washed with saline to remove adherent blood and then were placed on a microscope slide and imaged. Another microscope slide was then placed on top of the lobes, and the lobes were compressed to a thickness of 0.10 cm using spacers and an image was obtained. The slide was inverted and again imaged. The lobes were then compressed to a thickness of 0.072 cm, imaged, inverted, and imaged again.

Images were obtained as previously described. Briefly, a CRi Maestro system (Woburn, MA, USA) was used for multispectral acquisition and analysis, which was equipped with a 649 nm excitation filter and a 700 nm long pass emission filter. Images were acquired over the range of 700–800 nm in 10 nm increments and analysis was performed on those observed at 730 nm. Images of standard solutions held between microscope slides at a known thickness were taken each day to relate the observed intensity to the concentration of AlPCS.

Image-Pro Plus Version 6.3 (Media Cybernetics, Bethesda, MD, USA) was used to process the TIFF images, and the total number of pixels in the area of interest (AOI) and light energy referred to as the integrated optical density (IOD) were measured. The IOD represents the value of the total intensity of all pixels selected in the acquisition software. The IOD and number of pixels were exported to Excel for further processing. Pixel dimensions were calibrated at the specific level of magnification as described previously where there were 17.5 × 17.5 pixels in a square millimeter (Yi et al., 2010).

To estimate the concentration of AlPCS in each lobe, the numerical value of the integrated optical density, IOD, as assessed from digital images was normalized to the exposure time, T_e, and surface area, A, by converting to the light density, ρ, photons/unit area (or pixels)/unit time of exposure as shown earlier (Yi et al., 2010):

$$\rho = \frac{\mathrm{IOD}}{T_e \times A}$$

For solutions and tissues, respectively, the observed light density is given by the expressions below:

$$\frac{\mathrm{IOD}}{T_e \times A \times z} = KC$$

$$\frac{IOD}{T_e \times A \times z} = KC - \frac{KC\mu_t z}{2}$$

where K is the instrument constant for the conditions used for the lungs and was evaluated with standard solutions of known concentrations, C, exposure time, area, and thickness, z (Yi et al., 2010). Measuring the IOD as a function of tissue thickness allowed estimation of both the concentration and attenuation coefficient of lung samples, μ_t, from the slope, intercept, and independent measurement of the instrument constant.

To estimate the deposition fraction, the concentration in the lobe was multiplied by the estimated volume (product of thickness and area) to yield the mass deposited. The latter was divided by the inhaled mass, M_{inh}, to estimate the fraction of mass deposited in

Table 1
Data summary from aerosol exposures. Compiled data providing the type of device and solution used to generate the aerosol specifying the aerosol concentration (mass/volume of air, calculate from filter capture experiments) and particle size distribution (mass median aerodynamic diameter, MMAD, and geometric standard deviation, GSD). The lung volume, attenuation coefficient and concentration of AlPCS were derived from analysis of images obtained following exposure of mice to the aerosol and are reported as the mean ± standard deviation, $n = 3$.

Device	Solution	[Aerosol] (mg/L)	MMAD (μm)	GSD	Lung volume (μL)	Lung attenuation Coeff. (cm^{-1})	Lung [AlPCS] (μg/ml)
Jet	10 mg/ml AlPSC	0.14	0.20[b]	1.84	223 ± 25	10.2 ± 0.9	3.02 ± 0.73
Jet[a]	10 mg/ml AlPSC + 100 mg/ml CsCl	0.14	0.40[b]	1.81	243 ± 21	8.8 ± 1.4	2.07 ± 0.17
US	2 mg/ml AlPSC-silica column	0.20	0.42[c]	1.7	293 ± 48	10.0 ± 1.1	2.18 ± 0.39
US	2 mg/ml AlPSC + 18 mg/ml CsCl-silica column	0.52	1.1[c]	1.6	277 ± 4.2	11.0 ± 2.0	8.67 ± 4.31
US	2 mg/ml AlPSC	0.48	2.8[c]	2.0	256 ± 33	9.2 ± 1.8	0.95 ± 0.36

[a] Data taken from Yi et al.
[b] MMAD calculated from results from scanning mobility particle size measurement.
[c] MMAD obtained from cascade impactor.

each lobe. The total deposited mass was calculated from the sum of the mass deposited in each lobe. The inhaled mass was calculated from the following expression (Alexander et al., 2008):

$$M_{inh} = [Aer] \times RMV \times T_{inh}$$

where [Aer] is the aerosol concentration generated by the device, RMV is the respiratory minute volume of the mouse, and T_{inh} is the inhalation time during which the animals were exposed to the aerosol. The RMV was calculated from the formula provided by Alexander et al. (2008).

$$RMV = 0.608 \times BW^{0.852}$$

where BW is the body weight in kg and RMV is given in L/min, which was 22 ml for 20 g mice. No correction was made for the inhalable fraction. There are two components in the aerosol, AlPCS and CsCl, but only AlPCS is visible in the images. Thus, the aerosol concentration was based on the assay of AlPCS and was determined as follows. The mass of AlPCS collected on the filter, M_{fil}, was normalized by the collection time (t) and then divided by the air flow rate (Q, in LPM):

$$[Aer] = \frac{M_{fil}/t}{Q}$$

For assessing the uniformity of the deposition, the inherent broadening of the instrument was investigated by imaging a fluorophore solution contained within rectangular channels cut into opaque, black Plexiglas. The data was processed as described in Section 3 to yield the strength of the Gaussian filter that was then applied to the lung lobe images in ImagePro.

Results are reported as mean ± standard deviation with an $n = 3$, unless otherwise stated.

3. Results and discussion

Five different aerosols were generated to carry out the exposure in mice. The aerosol concentrations in terms of mass of AlPCS per volume of air (mg/L) are given in Table 1. It should be noted that certain aerosols also contained cesium chloride to allow examination of the effect of particle size. This is not included in the aerosol concentration in the table, since its presence was not detected in the fluorescent images. The M-N nebulizer is believed to generate droplets with a particle size near 1 μm, which were carried from the device at a flow rate of 2 LPM. The volume of the aqueous droplets produced in a minute was near 30 μl, which quickly evaporated leaving dry particles. The dry particles were thus composed of the non-volatile components, AlPCS or ALPCS with CsCl. The aerosol concentration in terms of AlPCS for both these systems was about 0.14 mg/L, calculated from the filter capture method.

The results from the SMPS provided an estimate of the particle size distribution. With the small initial droplet and the relatively low concentration of non-volatile solutes, small aerosol particles were obtained, which had a median particle size of 0.2 and 0.4 μm for the two different solutions, AlPCS and ALPCS with CsCl, respectively.

The US device generated droplets with an MMAD of 2.8 μm and a geometric standard deviation of 2.0. At an air flow rate of 0.5 LPM, the extent of evaporation is not significant in changing the particle size. With the larger initial droplets, the aerosol cloud carried a much higher mass in comparison to the jet nebulizer despite using a lower concentration of AlPCS in solution. Also important is the lower air flow rate, which contributed to the higher aerosol concentration. Two additional aerosols were generated with smaller particle size distributions by passing the droplets through a drying column. With a baffle solution containing 2 mg/ml of AlPCS, the particle size of the dried aerosol was 0.42 μm ± 1.7 (MMAD ± GSD). With the addition of cesium chloride to the AlPCS solution, the median aerosol particle size was near 1.1 μm ± 1.6.

Coincident with the larger particle size distributions, a higher aerosol concentration of fluorescent dye was produced. As given in Table 1, the aerosol concentration was 0.2, 0.52, and 0.48 mg/L based on dye content and ignoring the contribution from CsCl. The higher aerosol concentration has implications for the mass that can be delivered to the animal model. That is, the aerosol concentration generated with the US device was nearly four times greater than that produced by the M-N device, and this was accomplished with a solution that had one fifth of the concentration of AlPCS. Thus, based on the mass introduced into the devices, the US atomization process is nearly five times more efficient in the use of the compound. Nevertheless, if the CsCl was replaced with AlPCS, the aerosol concentration emanating from the Medi-Nuclear device could be potentially increased by a factor of 10.

A representative image of the five lobes and trachea of the mouse is given in Fig. 1. All light arises from AlPCS, since images of lobes without exposure to the AlPCS aerosol appear black using similar acquisition/processing conditions, reflecting the absence of tissue auto-fluorescence. The lobes were held between microscope slides to eliminate the curved surface that would cause light distortion secondary to reflection and the change in the refractive index between air and tissue. Such effects can be seen at the perimeter of the lobes, which appear as a bright halo. The Maestro imaging system contains multiple CCDs that simultaneously collect light at each pixel. Although there is a reduction in sensitivity compared to instruments that have a single CCD and collected light using a raster system, the depth of field is greater with the Maestro, which is more amenable to quantification.

The imaged area in pixels was converted to an area in square centimeter using the calibration of the pixels. This area when coupled to the compression thickness allowed calculation of the volume of each lobe. The results are given in Fig. 2, where the measured volume of the mouse lobes, L: left; RS: right superior; RM: right medial; RI: right inferior; PC: post claval; and T: trachea, for

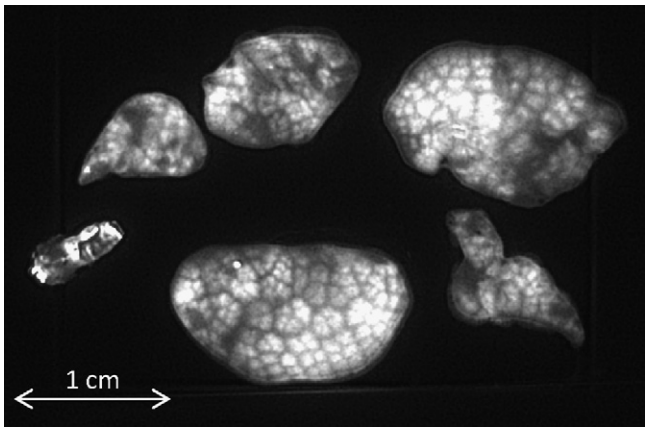

Fig. 1. Representative fluorescent image of the lobes and trachea of a mouse lung following exposure to an aerosol of AlPCS and compressed to a thickness of 0.1 cm.

the different aerosols is given. As expected, the observed volumes were uniform among the different exposures. It should be noted that this is the volume of a nearly collapsed lung. As such, the values fell between an expanded lung volume and a completely collapsed lung volume, estimated from the wet weight and unit density (Yi et al., 2010). The sum from all of the lobes provided a measure of the imaged lung volume (Table 1). This was consistent among the different exposures.

In our previous work (Yi et al., 2010), the relationship between the observed intensity in a fluorescent image arising from a solution of AlPCS was shown to be linearly related to the concentration over a specific range of concentrations, thickness (i.e., depth in a direction normal to the CCDs), and area. In such samples, there is no attenuation of the fluorescence. When the fluorescent molecules reside within tissue, there is loss of intensity due to reflection, refraction, scattering, and absorption. By acquiring images at different degrees of compression, it was possible to estimate the tissue attenuation of the fluorescent signal as well as the concentration. The fundamental assumptions are that the fluorescent dye is uniformly distributed in the tissue and that attenuation of light is a linear function of penetration depth. Despite the fact that

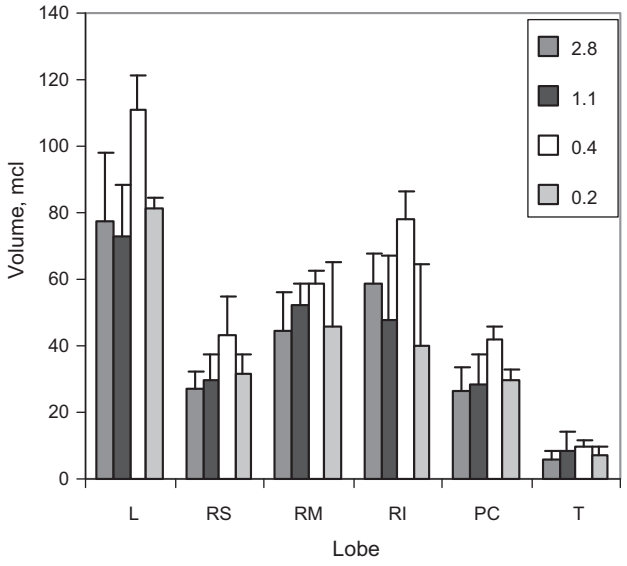

Fig. 2. Estimated lobe volumes (L: left; RS: right superior; RM: right medial; RI: right inferior; PC: post claval; T: trachea) obtained from image analysis following exposure to aerosols with median particle size of 0.2, 0.4, 1.1, and 2.8 μm. Results are expressed as the mean ± SD ($n = 3$).

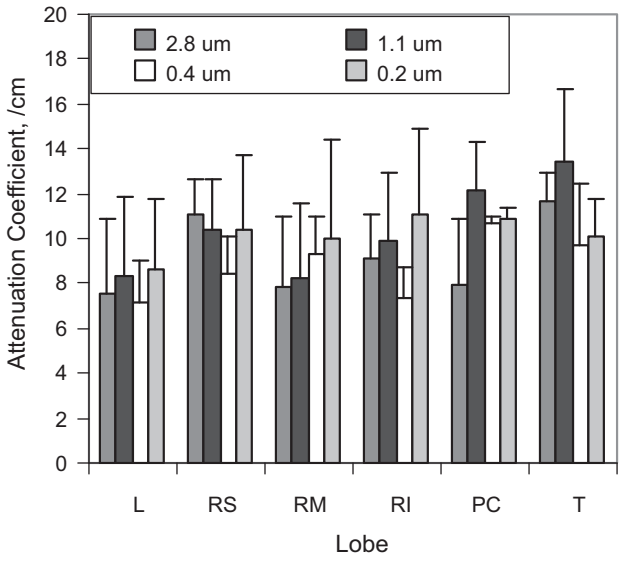

Fig. 3. Estimated attenuation coefficient of lobes (L: left; RS: right superior; RM: right medial; RI: right inferior; PC: post claval; and T: trachea) obtained from image analysis following exposure to aerosols with median particle size of 0.2, 0.4, 1.1, and 2.8 μm. Results are expressed as the mean ± SD ($n = 3$).

neither assumption is valid, the concentration estimated in the lobe was consistent with that measured in extracted solutions (Yi et al., 2010).

This approach was used to estimate the tissue attenuation for the different lobes and the results are given in Fig. 3. It can be seen that the values range from just over 6 to nearly 12 cm^{-1}, and the average for the entire lung is given in Table 1. These values did not depend on the particle size of the aerosol. The estimated AlPCS concentration in each lobe for the different aerosols is given in Fig. 4, and the total is also given in Table 1. For each aerosol, the concentration among the different lobes was very similar. Among the different sized aerosols, the lowest concentration was observed with the 2.8 μm particles, which was at and below 1 μg/ml. Despite the relatively high aerosol concentration for this aerosol, little mass reached the lower respiratory tract.

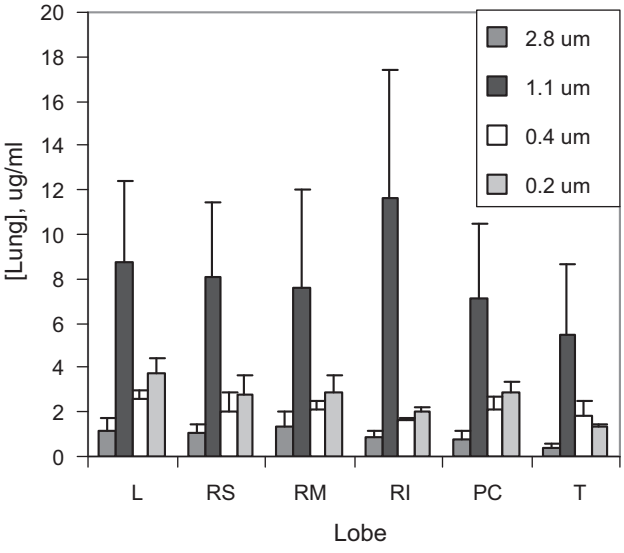

Fig. 4. Estimated AlPCS concentration in the lobes (L: left; RS: right superior; RM: right medial; RI: right inferior; PC: post claval; T: trachea) obtained from image analysis following exposure to aerosols with median particle size of 0.2, 0.4, 1.1, and 2.8 μm. Results are expressed as the mean ± SD ($n = 3$).

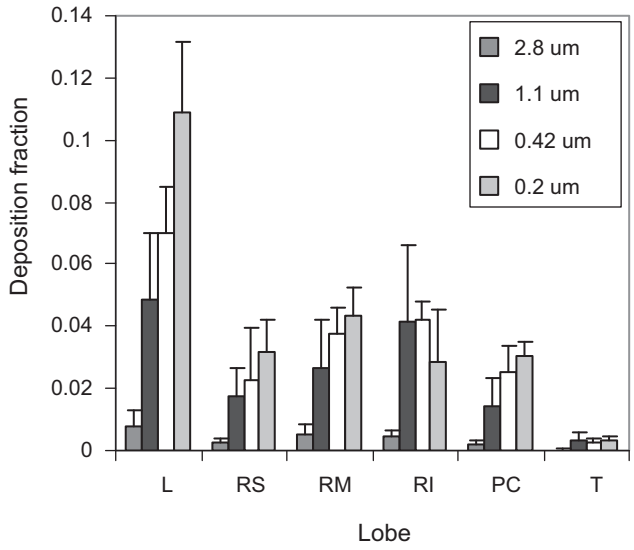

Fig. 5. Estimated deposition fraction of AlPCS in the lobes (L: left; RS: right superior; RM: right medial; RI: right inferior; PC: post claval; T: trachea) obtained from image analysis following exposure to aerosols with median particle size of 0.2, 0.4, 1.1, and 2.8 μm. Results are expressed as the mean ± SD ($n = 3$).

The 0.2 and 0.4 μm aerosols gave rise to concentrations near 3 μg/ml and 2 μg/ml. Since they both had similar aerosol concentrations, the higher concentration observed with the smaller aerosol particle size can be ascribed to a higher deposition fraction. The highest concentrations of AlPCS in the lobes were observed with the 1 μm aerosol and varied between 6 and nearly 12 μg/ml. This reflects the optimal combination of a high aerosol concentration of AlPCS and a reasonably high deposition fraction.

From the measured lobe volumes and AlPCS concentration, the deposited mass was calculated. By normalizing to the inhaled mass, the deposition fraction was estimated (Fig. 5). The calculation of the inhaled mass depends on the estimate of the respiratory minute volume, which in turn depends on the formula selected (Alexander et al., 2008). Inherent in this approach is the potential for a systematic error, where the RMV may not be appropriate for the mice and conditions of exposure used in this study. Nevertheless, since the concentrations were relatively uniform among the lobes, it can be concluded that the deposition fraction, that is, the mass of the inhaled aerosol that deposited in a given lobe increased with lobe size. Thus, the left lobe is the largest and thereby has the largest deposited mass fraction.

Examining the fractions in the left lobe for the different aerosols, low values were observed with the 2.8 μm aerosol, generally less than 1%. With a decrease in particle size, the fraction increased to 5% at 1 μm, 8% at 0.4 μm, and nearly 11% at 0.2 μm. This rank order was also observed for the right medial and post claval lobes. For the remaining two lobes and the trachea, the 0.2 μm aerosol had slightly lower deposition fractions than the 0.4 μm aerosol.

These values are low in comparison to the published work by Raabe et al. (1988) and may reveal invalid assumptions. The advantage of using hand-held mice and a short exposure time is that there is a well defined start and stop time, and the distribution of compound into the blood stream can be neglected. On the other hand, there is concern from the use of hand-held animals during the exposure in that the deposition may be adversely affected and unwanted variability may have occurred. It should also be noted that no effort was made to quantify the extrathoracic deposition of the fluorescent dye, which would be expected to be significant particularly with the aerosols with a larger particle size distribution. The incompressibility of the boney nasal cavity coupled with poor light penetrability appeared to pose insurmountable problems for this approach.

To examine the distribution of AlPCS within the lung, we focused on the left lobe. Here, it must be appreciated that in addition to loss of light by the above mechanisms, there is also distortion. That is, images obtained with the Maestro system do not appear sharply focused because tissue affects the path of light by reflection, refraction and scattering (Kovar et al., 2007; Comsa et al., 2008). This in turns causes photons to be accumulated in a CCD that is not directly above the rectangular prism of the tissue.

While there is a sophisticated approach that separates direct incident light from scattered light, the solution used here was to empirically determine the resolution enhancement needed to correct for light distortion (Ntziachristos et al., 2008). To identify an appropriate approach to increase the resolution of the lung images without incurring inappropriate light distortion, an image of a solution of AlPCS contained within a rectangular channel was obtained. The values of intensity were obtained along a line on the image perpendicular to the channel length and were plotted as a function of pixel number. This is shown in Fig. 6A. The far right curve is the uncorrected data, which appears as a Gaussian broadened curve. This is consistent with the work from Comsa et al. (2008), which indicated that light distortion can be modeled a random process.

As can be seen, the curve rises from near zero at a point distant from the channel, which corresponds to the background signal, to the maximum value, which corresponds to the AlPCS contained within the center of the channel. The solid line represents a best fit to a Gaussian function where the standard deviation was allowed to vary. Thereafter, a Gaussian filter with a specified strength was applied to a grouping of 9 by 9 square of pixels in the image, and again the data of a line cut was plotted and fit. This is shown in Fig. 6A, where each curve moving from right to left became steeper as a Gaussian function of greater strength was applied. However, at strength 8, the intensity within the channel no longer appeared as a plateau, which indicates that the light intensity was distorted. In the companion Fig. 6B, the fitted standard deviation is given as a function of Gaussian strength. The initial, uncorrected figure required a standard deviation over three, whereas at a strength of 6, the standard deviation required to fit the curve was reduced to just over 1.5.

Based on the effect of the correction on image resolution, a Gaussian filter of strength 6 for each 9×9 pixel group was applied to the images of the lung lobes. Representative images of the left lobe are shown in Fig. 7. The gray scale has been adjusted so that the brightest region in each lobe has a similar appearance. It perhaps is important to note that the image of any lobe arises exclusively from variations in the intensity of AlPCS, since the background tissue fluorescence is negligible. Moreover, within each lobe, the observed intensity is a function of the concentration of AlPCS and the extent of attenuation.

As an example, consider the top left image that was obtained with the 0.2 μm sized aerosol. Here, the top central portion appears darker, with an evident channel extending from the top towards the lower portion of the lobe and to the left. This corresponds to where the main airway would be expected to be in the left lobe of the lung. There are also specific dark, nearly circular regions along a linear path and in isolated regions. These corresponded to places where clotted blood was visually evident at the surface of the lobes. The network of smaller dark lines seen throughout the lobes in the images arises from primarily the connective tissue and blood vessels and not airways. From the dimensions of the network, clusters of alveoli would be located between these dark-lined branches. With more sophisticated approaches to exsanguination and processing of the excised lobes, artifacts from blood can be minimized and possibly eliminated.

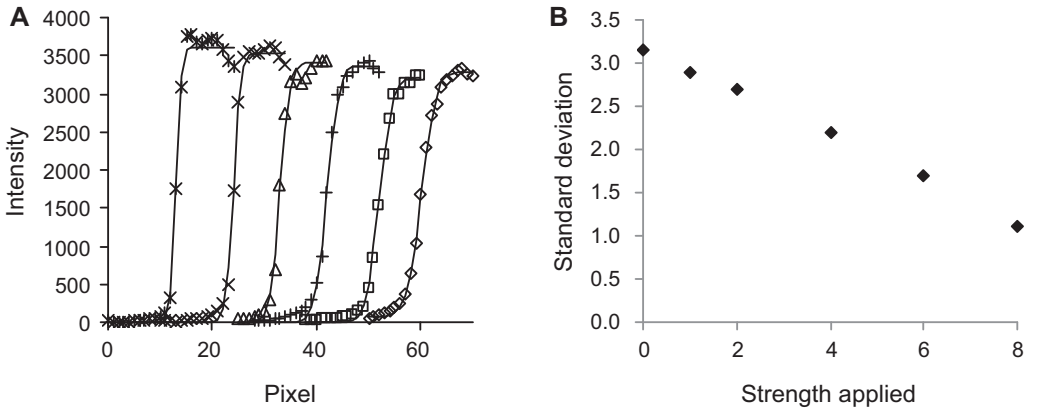

Fig. 6. (A) Fluorescent intensity given as a function of pixel obtained from analysis of a line cut of an image of AlPCS contained within a rectangular channel with no correction (◊) and with a Gaussian correction of strength 1 (□), 2 (+), 4 (△), 6 (×), and 8 (*) applied once to a 9 × 9 group of pixels. The solid lines represent best fits of the data to a Gaussian function. (B) Best fit standard deviation applied to data in (A) following application of a Gaussian correction of the indicated strength.

The images in the left column were obtained at a compression thickness of 0.1 cm. In comparing the images in the left column, there does not appear to be any stark differences in terms of the distribution of the intensity for these images despite that fact that the aerosol particle size ranged over an order of magnitude from 0.2 μm (top) to 2.8 μm (bottom). With closer examination of the image obtained, at 1.1 μm, the large tubular structure arising from the main airways was not evident as in the lungs exposed to the other aerosols.

The images obtained at a compression thickness of 0.072 cm are shown in the center column after they were adjusted by resizing so that the width of the image of the lobe contained the same number

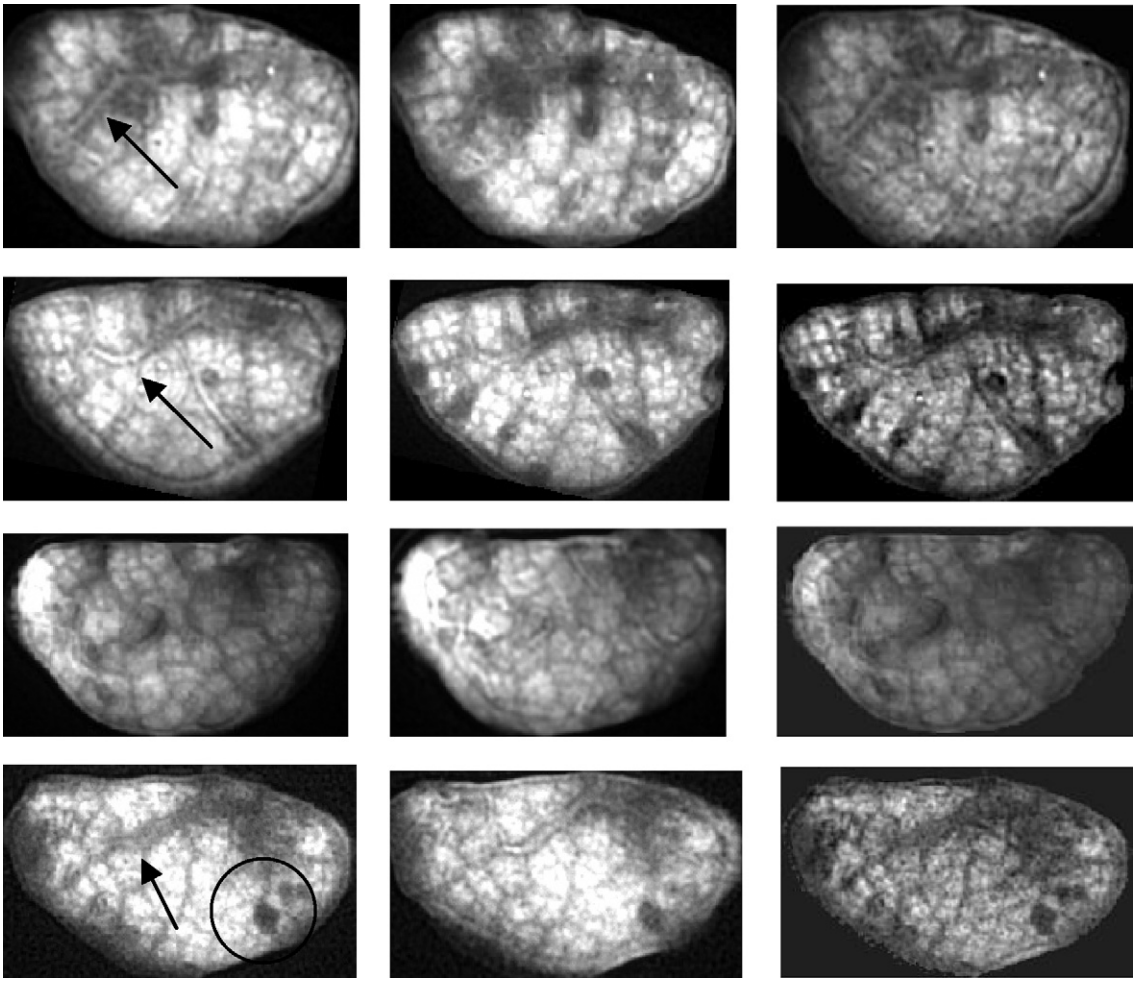

Fig. 7. Fluorescent images of the left lobe following aerosol exposure to AlPCS particles. The first row was obtained with a 0.2 μm aerosol, second row with a 0.4 μm, third row with a 1.1 μm and bottom row with a 2.8 μm aerosol. The first column of images were obtained with a compression thickness of 0.1 cm, the middle column was obtained with a compression thickness of 0.072 cm, and the third column are images of the relative concentration estimated from image analysis. The arrows indicate the large airways visible in the 0.2, 0.4, and 2.8 μm aerosol. The circle encloses dark spots arising from clotted blood.

of pixels as that obtained at a thickness of 0.1 cm (left). This was necessary to permit alignment of the two images for further processing as discussed below. While it is obvious these images were taken of the same lobe, because of the slight distortion caused by the compression of the tissue and the slight displacement of the sample relative to the camera view, perfectly exact alignment was not possible to achieve for these images. Although not shown, the network of dark lines also does not exactly correspond between the top and bottom views of the same lobe. This is perhaps expected, since the lung tissue provides mechanical support to groups of alveoli, clustered like grapes, and as such, would not extend from one side of the lobe to the exact same position on the other side. Whereas the size of each image has been adjusted to be equal, the actual dimensions can be deduced from the number of pixels, which has been measured to be 17.5×17.5 pixels/square millimeter in images in the left hand column. The size of one alveoli of CL mice has been reported to be about 50 μm (Soutiere et al., 2004), which would occupy about four pixels in the x–y plane of the image. The thickness of the tissue is either 720 or 1000 μm, in the z-axis, which is taken to be normal to the surface. Thus, about 20 alveoli are seen as a two dimensional projection with the passage of light through the tissue.

For processing, the intensity value at each pixel or the bitmap was exported to an Excel file. With the image data sets obtained at 0.1 and 0.07 cm, the intensity as a function of compression thickness was extrapolated to zero thickness at each pixel. As given in Section 2, the slope of the extrapolation is related to the attenuation and the intercept is related to the concentration. The right hand column contains images that were obtained by exporting the Excel file containing the value of concentration to the program, ImageJ, which generates a figure from the bitmap values. Again, the intensity has been scaled to a grey scale that can be seen by eye and thus while the relative intensity of each figure is representative of the relative concentration, the same intensity in different figures is not derived from the same concentration.

Comparing the figures of concentration with that representing intensity, they appear very similar. However, it is noted that the figures of the concentration have less variability in appearance as those of intensity. That is, the dark regions have been brightened and the bright regions are less so. This is also reflected in a comparison of the values of the relative standard deviation of the intensity and concentration that was calculated from the excel table of concentration. This was a consequence of the correction for the attenuation. Thus for example, the apparent portion of the intensity image arising from the main airway was darker due to a somewhat larger attenuation and therefore appears slightly brighter in the concentration image. In the same way, the bright regions corresponding to the groups of alveoli sacs had less attenuation and this appears less bright. Nevertheless, this represents only a minor contribution, since the overall appearance remains larger unchanged.

With the images reflective of concentration, a relatively detailed image is still apparent. The dark network of lines arising from the connective tissue remain in the image, which evidently has a much lower concentration of fluorescent probe compared with the central airways and alveoli. This may have implications for the treatment of fibrotic lung disease. However, this approach does not allow the deposition in small airways to be distinguished from deposition in the alveoli. The appearance of the left lobes following exposure to aerosols with different particle sizes can be examined in more detailed. Perhaps of greatest interest is the appearance of the central, larger airway, which is clearly evident with three of the exposures but remains obscured with the exposure to the 1.1 μm aerosol. This observation would be consistent with a more uniform distribution of fluorescent particles with the intermediate particle size in comparison to the larger and smaller aerosols.

Finally, the magnitude of the attenuation coefficient can be considered in the context of the images. With a value of $10\,cm^{-1}$, the intensity falls exponentially such that at a thickness of 0.1 cm, only 1/e or 37% of the light will pass through the tissue. By viewing from both the top and bottom perspectives, this loss is minimized since 60% of the light would reach the surface if emanating from a depth of 0.05 cm. Nevertheless, interpretation of these two perspectives is more complex, since there are now overlapping signals, which perhaps requires consideration of the geometric mean to estimate the total intensity (Xia et al., 2008).

4. Conclusion

With the above approach, relatively high resolution images of mouse lungs were obtained. As such, this provides a means for obtaining detailed analysis of the distribution of deposited aerosol particles. Moreover, it is reasonably fast and economical, allowing large number of animals to be studied. Since it is carried out in the mouse, which is used as a model for many diseases, concentration of aerosol particles at the site of disease, for example a cancerous nodule, can be readily assessed. Finally, the effects of altered lung structure on particle deposition can also be studied in greater detail.

Conflict of interest

Amir Naqwi was principal investigator on NIH grant HL081789, and Timothy Wiedmann was a collaborating investigator and has served as a consultant to Powerscope Inc. Dandan Yi has no potential conflicts of interest.

Acknowledgments

We would like to thank Andrew Price and Angela Panoskaltsis-Mortari for assisting us early on in the imaging of mouse lungs. Dandan Yi was supported by the China Scholarship Council. In addition, Andrew Clarke, Logan Brentley, Na Young Kim, and Makin Osman expended effort in analyzing images. The work was supported in part by NIH grant HL081789 awarded to Powerscope Inc.

References

Adams, K.E., Ke, S., Kwon, S., Liang, F., Fan, Z., Lu, Y., Hirschi, K., Mawad, M.E., Barry, M.A., Sevick-Muraca, E.M., 2007. Comparison of visible and near-infrared wavelength-excitable fluorescent dyes for molecular imaging of cancer. J. Biomed. Opt. 12, 102–117.

Alexander, D.J., Collins, C.J., Coombs, D.W., Gilkison, I.S., Hardy, C.J., Healey, G., Karantabias, G., Johnson, N., Karlsson, A., Kilgour, J.D., McDonald, P., 2008. Association of Inhalation Toxicologists (AIT) working party recommendation for standard delivered dose calculation and expression in non-clinical aerosol inhalation toxicology studies with pharmaceuticals. Inhal. Toxicol. 20, 1179–1189.

Chen, T.W., Lin, B.J., Brunner, E., Schild, D., 2006. In situ background estimation in quantitative fluorescence imaging. Biophys. J. 90, 2534–2547.

Comsa, D.C., Farrell, T.J., Patterson, M.S., 2008. Quantitative fluorescence imaging of point-like sources in small animals. Phys. Med. Biol. 53, 5797–5814.

Dolovich, M.B., 2009. 18F-fluorodeoxyglucose positron emission tomographic imaging of pulmonary functions, pathology, and drug delivery. Proc. Am. Thorac. Soc. 6, 477–485.

Eberl, S., Chan, H.K., Daviskas, E., 2006. SPECT imaging for radioaerosol deposition and clearance studies. J. Aerosol. Med. 19, 8–20.

Jaafar-Maalej, C., Andrieu, V., Elaissari, A., Fessi, H., 2009. Assessment methods of inhaled aerosols: technical aspects and applications. Expert Opin. Drug Deliv. 6, 941–959.

Kovar, J.L., Simpson, M.A., Schutz-Geschwender, A., Olive, D.M., 2007. A systematic approach to the development of fluorescent contrast agents for optical imaging of mouse cancer models. Anal. Biochem. 367, 1–12.

Martin, A.R., Thompson, R.B., Finlay, W.H., 2008. MRI measurement of regional lung deposition in mice exposed nose-only to nebulized superparamagnetic iron oxide nanoparticles. J. Aerosol Med. Pulm. Drug Deliv. 21, 335–342.

Mohajerani, P., Adibi, A., Kempner, J., Yared, W., 2009. Compensation of optical heterogeneity-induced artifacts in fluorescence molecular tomography: theory and in vivo validation. J. Biomed. Opt. 14, 034021.
Ntziachristos, V., Culver, J., Rice, B.W., 2008. Small-animal optical imaging. J. Biomed. Opt. 13, 011001.
Raabe, O.G., Al-Bayati, M.A., Teague, S.V., Rasolt, A., 1988. Regional deposition of inhaled monodisperse coarse and fine aerosol particles in small laboratory animals. Ann. Occup. Hyg. 32, 53–63.
Rostami, A.A., 2009. Computational modeling of aerosol deposition in respiratory tract: a review. Inhal. Toxicol. 21, 262–290.
Soutiere, S.E., Tankersley, C.G., Mitzner, W., 2004. Differences in alveolar size in inbred mouse strains. Respir. Physiol. Neurobiol. 140, 283–291.
Weers, J., Metzheiser, B., Taylor, G., Warren, S., Meers, P., Perkins, W.R., 2009. A gamma scintigraphy study to investigate lung deposition and clearance of inhaled amikacin-loaded liposomes in healthy male volunteers. J. Aerosol Med. Pulm. Drug Deliv. 22, 131–138.
Xia, Z., Huang, X., Zhou, X., Sun, Y., Ntziachristos, V., Wong, S.T., 2008. Registration of 3-D CT and 2-D flat images of mouse via affine transformation. IEEE Trans. Inf. Technol. Biomed. 12, 569–578.
Xie, Y., Zeng, P., Wiedmann, T.S., 2008. Disease guided optimization of the respiratory delivery of microparticulate formulations. Exp. Opin. Drug Deliv. 5, 269–289.
Xie, Y., Longest, P.W., Xu, Y.H., Wang, J.P., Wiedmann, T.S., 2010. In vitro and in vivo lung deposition of coated magnetic aerosol particles. J. Pharm. Sci. 99, 4658–4668.
Yi, D., Price, A., Panoskaltsis-Motari, A., Naqwi, A., Wiedmann, T.S., 2010. Measurement of the distribution of aerosols among mouse lobes by fluorescent imaging. Anal. Biochem. 403, 88–93.